Journal of Computational Physics **149,** 168–193 (1999)
Article ID jcph.1998.6136, available online at http://www.idealibrary.com on IDEAL®

# A Conservative Finite Difference Method for the Numerical Solution of Plasma Fluid Equations[1]

Phillip Colella,* Milo R. Dorr,† and Daniel D. Wake†

**Lawrence Berkeley National Laboratory, One Cyclotron Road, MS 50D, Berkeley, California 94720;*
†*Lawrence Livermore National Laboratory, P.O. Box 808, L-561, Livermore, California 94551*
E-mail: MiloDorr@llnl.gov

Received April 14, 1998; revised October 9, 1998

This paper describes a numerical method for the solution of a system of plasma fluid equations. The fluid model is similar to those employed in the simulation of high-density, low-pressure plasmas used in semiconductor processing. The governing equations consist of a drift-diffusion model of the electrons, together with an internal energy equation, coupled via Poisson's equation to a system of Euler equations for each ion species augmented with electrostatic force, collisional, and source/sink terms. The time integration of the full system is performed using an operator splitting that conserves space charge and avoids dielectric relaxation timestep restrictions. The integration of the individual ion species and electrons within the time-split advancement is achieved using a second-order Godunov discretization of the hyperbolic terms, modified to account for the significant role of the electric field in the propagation of acoustic waves, combined with a backward Euler discretization of the parabolic terms. Discrete boundary conditions are employed to accommodate the plasma sheath boundary layer on underresolved grids. The algorithm is described for the case of a single Cartesian grid as the first step toward an implementation on a locally refined grid hierarchy in which the method presented here may be applied on each refinement level. 

*Key Words:* models; numerical methods; finite difference methods; ionized gas flow in electromagnetic fields; plasmic flow.

## 1. INTRODUCTION

Many plasma phenomena can be predicted using mathematical models in which the plasma is treated as a fluid comprised of charged species. One example is provided by

[1] This work was supported by the Applied Mathematical Sciences Program of the Office of Mathematics, Information and Computational Sciences, of the U.S. Department of Energy under Contract DE-AC03-76SF00098 with Lawrence Berkeley National Laboratory and by Lawrence Livermore National Laboratory under Contract W-7405-Eng-48.



0021-9991/99 $30.00

models of industrial plasmas used in the manufacture of very large scale integrated (VLSI) circuits. Inductively coupled plasma (ICP) reactors are one type of tool designed to satisfy the demanding process requirements resulting from the desire to create increasingly smaller device features on increasingly larger wafers. In spite of the low pressures employed in ICP reactors, the numerical solution of systems of equations arising from fluid models of these plasmas can be very effective in predicting some important aspects of their behavior, such as the uniformity of the plasma across the wafer [13].

One of the challenges in the computational modeling of high-density, low-pressure process plasmas is the presence of boundary layers, called *sheaths*. As in other types of boundary layer problems, there are two main ways to account for sheaths. One approach is to explicitly include a boundary layer expansion obtained from one-dimensional scaling analyses normal to the boundary. These expansions are coupled to simulations of the bulk plasma by enforcing compatibility conditions, such as continuity of fluxes and fields, at the boundary separating the two models. The combination of sheath and bulk models is the standard approach currently used in industrial plasma simulators.

A second generic method for handling boundary layers is the use of local grid refinement. In this approach, fine grids are deployed in regions of high estimated error and/or solution variation (e.g., the sheath) while coarser grids are used in the more quiescent regions (e.g., the bulk plasma). The flexibility and gains in resolution provided by local mesh refinement are further enhanced when combined with high-order discretization methods yielding smaller discretization errors per grid cell than conventional first-order methods, thereby reducing the amount of grid refinement needed to achieve a given level of accuracy. High-resolution methods combining high-order discretization and local grid refinement have been extremely successful in solving systems of equations arising from computational models of neutral fluids, including those admitting viscous boundary layers.

The purpose of this paper is to begin the development and analysis of high-resolution methods for the solution of a plasma fluid system representative of those describing the high-density, low-pressure process plasmas mentioned above. In this first step, we consider a model in which the plasma is regarded as a multicomponent fluid comprised of ions and electrons, coupled by Poisson's equation. The motion of the electrons is described by a drift-diffusion model, together with an internal energy equation, while each ion species is modeled using the classical Euler equations of gas dynamics augmented with electrostatic force, collisional, and source/sink terms. We describe and analyze a discretization method in which the plasma components are integrated in a time-split manner that conserves space charge and avoids *dielectric relaxation* timestep restrictions. For the integration of the individual ion species and electrons, a second-order Godunov discretization is applied to the hyperbolic terms, with appropriate modifications made to account for the significant role of the electric field in the propagation of acoustic waves. The parabolic terms are integrated using backward Euler, although higher-order backward difference formulas could also be used. Discrete boundary conditions are imposed in a manner consistent with the well-known Bohm criterion for the minimum ion velocity at the sheath boundary, together with a boundary condition on the electron flux designed to yield a self-consistent value, regardless of whether or not the sheath is resolved.

In this discussion, we restrict our attention to the case of a single Cartesian grid, or by a straightforward extension, an arbitrary union of Cartesian grids. As suggested above, however, our ultimate goal is to incorporate a local mesh refinement strategy. One approach to integrating a fluid system on block-structured locally refined grids is to regard the structure

as a hierarchy of refinement levels, each of which is an arbitrary union of Cartesian grids appropriately nested in the next coarser level. Time integration can then be performed on a level-by-level basis, combined with synchronizations to enforce interlevel compatibility conditions. A fundamental requirement in such an approach is an effective algorithm to integrate the fluid system on a single refinement level, which is the topic of this paper. The algorithmic issues arising even in this restricted context are sufficient to warrant their specific consideration here, deferring the description of the algorithm on locally refined grids to a subsequent article [4].

In Section 2, we present the physical model and the resulting system of equations to be solved. Section 3 begins with a discussion of some essential model characteristics and mathematical issues affecting the choice of discretization method. Each step of the time-split integration method is then described in detail. Some numerical results illustrating the computational complexity and convergence of the method are then presented in Section 4.

## 2. PLASMA FLUID MODEL

The governing equations for a plasma fluid model are based on Maxwell's equations, together with moments of the Boltzmann equations describing the transport of the ion and electron components. Each plasma component is assumed to have a drifting, near-Maxwellian velocity distribution. The infinite set of moment equations is truncated, and the moments corresponding to the conservation of mass, momentum, and energy for each component are retained. A detailed development can be found in [8]. In our model, each ion species $i$ is modeled by the system

$$\frac{\partial n_i}{\partial t} + \nabla \cdot (n_i u_i) = \sum_j R_{ij}, \tag{2.1}$$

$$\begin{aligned}\frac{\partial (m_i n_i u_i)}{\partial t} &+ \nabla \cdot (m_i n_i u_i u_i) + \nabla (n_i k T_i) \\ &= q_i n_i E - \sum_j \frac{m_i m_j}{m_i + m_j} n_i \nu_{ij} (u_i - u_j) + \sum_{j|R_{ij}<0} m_i u_i R_{ij} + \sum_{j|R_{ij}>0} m_i u_j R_{ij},\end{aligned} \tag{2.2}$$

$$\begin{aligned}\frac{\partial}{\partial t}\left[n_i\left(\frac{m_i}{2} u_i \cdot u_i + \mathcal{E}_i\right)\right] &+ \nabla \cdot \left[n_i\left(\frac{m_i}{2} u_i \cdot u_i + \mathcal{E}_i\right) u_i\right] + \nabla \cdot (n_i k T_i u_i) = q_i n_i u_i \cdot E \\ &- \sum_j \frac{2 m_i m_j}{(m_i + m_j)^2} n_i \nu_{ij} \left[\frac{1}{2}(m_i u_i \cdot u_i - m_j u_j \cdot u_j + (m_j - m_i) u_i \cdot u_j) + \mathcal{E}_i - \mathcal{E}_j\right] \\ &+ \sum_{j|R_{ij}<0} \left(\frac{m_i}{2} u_i \cdot u_i + \mathcal{E}_i\right) R_{ij} + \sum_{j|R_{ij}>0} \left(\frac{m_j}{2} u_j \cdot u_j + \mathcal{E}_j\right) R_{ij} + \sum_j \epsilon_{ij} S_{ij},\end{aligned} \tag{2.3}$$

$$\mathcal{E}_i = \frac{k T_i}{\gamma_i - 1}, \tag{2.4}$$

whose variables are defined in Table I. The summation notation in the right-hand sides of (2.2) and (2.3) denotes summation over all particle species (electron, ion, and neutral). The equations (2.1)–(2.4) are the classical Euler equations for a polytropic ideal gas augmented by electrostatic force, collisional, and gain/loss terms.

The electron equations are obtained from a moment system analogous to (2.1)–(2.4) with a number of additional assumptions. First, we assume the drift-diffusion approximation for

**TABLE I**
**Variables Used in the Plasma Fluid Model**

| | |
|---|---|
| $n_j$ | Number density |
| $u_j$ | Velocity |
| $\phi$ | potential |
| $E$ | Electric field |
| $T_j$ | Temperature |
| $\mathcal{E}_j$ | Internal energy |
| $\gamma_j$ | Ratio of specific heats |
| $P_{\text{ind}}$ | Input power density |
| $\mu, \eta$ | Transport coefficients |
| $m_j$ | Mass |
| $R_{ij}$ | Number density gain/loss rates from ionization, attachment, etc. |
| $S_{ij}$ | Number density gain/loss rates from inelastic collisions |
| $\epsilon_{ej}$ | Energy transferred in inelastic collisions |
| $\nu_{ij}$ | Elastic collision frequencies |
| $q_j$ | Charge |
| $e$ | Elementary charge |
| $\epsilon_0$ | Permittivity of free space |
| $k$ | Boltzmann's constant |

the electron directed velocity. This approximation is sometimes referred to as the zero mass approximation, but actually it is just the elimination of inertial terms that are negligible, provided that the electron plasma oscillations are not resolved. The result is the replacement of the electron momentum equation with an equation of state for the electron flux determined from a balance of forces. The system of electron equations we consider is, therefore,

$$\frac{\partial n_e}{\partial t} + \nabla \cdot (n_e u_e) = \sum_j R_{ej}, \tag{2.5}$$

$$n_e u_e = -\mu n_e E - \eta \nabla (n_e k T_e), \tag{2.6}$$

$$\frac{\partial \left(\frac{3}{2} n_e k T_e\right)}{\partial t} + \nabla \cdot \left( n_e \frac{5}{2} k T_e u_e \right)$$
$$= -e n_e u_e \cdot E + \nabla \cdot \left( \frac{5\eta}{2} n_e k T_e \nabla k T_e \right) + P_{\text{ind}} - \sum_j \frac{3 m_e}{m_j} k T_e \nu_{ej} n_e + \sum_j \epsilon_{ej} S_{ej}, \tag{2.7}$$

where

$$\nu_{en} \equiv \sum_j \nu_{ej}, \tag{2.8}$$

$$\mu \equiv e / m_e \nu_{en}, \tag{2.9}$$

$$\eta \equiv 1 / m_e \nu_{en} \tag{2.10}$$

and the remaining variables are defined in Table I. Equation (2.7) for the electron internal energy density, $\frac{3}{2} n_e k T_e$, is obtained by combining (2.5) and (2.6) with the equation for the total electron energy. The remaining approximations made in (2.5)–(2.8) are based on the low electron mass and (assumed) high electron temperature, relative to those of the other particle species.

The coupling of external power to the plasma is via the deposition source term $P_{\text{ind}}$ in the electron energy equation (2.7). We assume that this source term is known *a priori* rather than include a full electromagnetic model. For ICP applications, the high thermal conductivity of the plasma, along with the skin depth-limited penetration of electromagnetic fields, makes the decoupling of the source and plasma a reasonable approximation, provided the region of interest is more than a few skin depths away from the coils (typically a few centimeters). With this simplification and the absence of external magnets, we may neglect magnetic fields. The electromagnetic behavior is then simply described by Poisson's equation

$$\epsilon_0 \nabla \cdot E = \sum_i q_i n_i + q_e n_e, \quad E = -\nabla \phi. \tag{2.11}$$

Boundary conditions for the system (2.1)–(2.11) will be specified in Section 3.3 in the context of our numerical discretization.

## 3. NUMERICAL ALGORITHM

### 3.1. *Motivation*

Before describing our numerical algorithm, we consider the plasma characteristics and mathematical issues that affect the discretization.

The slow motion of the ions, relative to the electrons, allows some flexibility in the manner in which they are advanced. We do, however, want to retain high spatial accuracy. Regarding the right-hand sides as source terms, (2.1)–(2.4) are the inhomogeneous Euler equations of gas dynamics. The mathematical properties of such equations are well understood for a neutral gas for which effective high-order numerical methods have been developed [3].

As part of the plasma fluid system, the ion equations differ from those describing a neutral gas in at least one important respect, however. Derivations of the dispersion relations for positive ion acoustic waves (e.g., [2]) reveal that the second term in the right-hand side of (2.2), involving the field $E$, makes a significant contribution to the plasma sound speed if $T_e \gg T_i$. Specifically, it is seen that small-amplitude, low-frequency waves propagate with speed $\sqrt{(kT_e + \gamma_i kT_i)/m_i}$ rather than the neutral sound speed $\sqrt{\gamma_i kT_i/m_i}$. This is even more evident in the case of ambipolar flow [2] for which

$$E = \frac{\mu_i kT_i - \mu_e kT_e}{e(\mu_i + \mu_e)} \frac{\nabla n_i}{n_i} \approx -\frac{kT_e}{e} \frac{\nabla n_i}{n_i} \tag{3.12}$$

(assuming that the electron mobility $\mu_e \equiv e/m_e \nu_{en}$ dominates the ion mobility $\mu_i \equiv e/m_i \nu_{in}$), which implies that the second term in the right-hand side of (2.2), containing the field $E$, dominates the ion pressure gradient. This important fact must therefore be included in the hyperbolic discretization. We accomplish this by explicitly incorporating the plasma sound speed in the left-hand side of the equations for the positive ion species with a corresponding modification of the source terms. In convective form, the positive ion momentum equations then become

$$n_i \frac{Du_i}{Dt} + \frac{\gamma_i kT_i + kT_e}{m_i} \nabla n_i = S_i, \tag{3.13}$$

where

$$\frac{Du_i}{Dt} \equiv \frac{\partial u_i}{\partial t} + (u_i \cdot \nabla)u_i, \tag{3.14}$$

$$S_i \equiv \frac{kT_e}{m_i}\nabla n_i + \frac{q_i n_i}{m_i}E - \sum_j \frac{m_j n_i \nu_{ij}}{m_i + m_j}(u_i - u_j) + \sum_{j|R_{ij}<0} u_i R_{ij} + \sum_{j|R_{ij}>0} u_j R_{ij}. \tag{3.15}$$

For electropositive systems (i.e., all ion species are positive), we employ the rearrangement (3.13) for each ion species. For electronegative systems (i.e., plasmas with at least one negative ion species) we retain the original form of (2.2) for each negative ion species and replace (3.13) for each positive ion species by

$$n_i \frac{Du_i}{Dt} + \frac{\gamma_i kT_i + \beta kT_e}{m_i}\nabla n_i = S_i, \tag{3.16}$$

$$S_i \equiv \frac{\beta kT_e}{m_i}\nabla n_i + \frac{q_i n_i}{m_i}E - \sum_j \frac{m_j n_i \nu_{ij}}{m_i + m_j}(u_i - u_j) + \sum_{j|R_{ij}<0} u_i R_{ij} + \sum_{j|R_{ij}>0} u_j R_{ij}, \tag{3.17}$$

where, letting $N$ denote the set of indices corresponding to the negative ion species,

$$\beta \equiv \frac{1 + \sum_{i\in N}\alpha_i}{1 + \sum_{i\in N}\alpha_i \frac{T_e}{T_i}}, \quad \alpha_i \equiv \frac{n_i}{n_e}. \tag{3.18}$$

The use of the factor $\beta$ to modify the Bohm criterion for sheath formation in the presence of negative ion species is described in Section 6.4 of [11]. We have employed a similar argument here to reduce the electronegative plasma sound speed.

The ion energy equations (2.3) are modified in a manner consistent with the corresponding momentum equations. The complete system is given in Section 3.2.1 below.

The rearrangement (3.13) was performed to introduce explicitly the correct plasma sound speed (as indicated by a linear analysis) in the left-hand side of the fluid system, allowing the right-hand side to be treated as a lagged source term in an explicit integration of the full nonlinear system. We now show that the momentum source (3.15) does in fact vary slowly, relative to the plasma sound speed time scale. In this analysis, we consider a single, positive ion species and assume that the electron temperature $T_e$ is constant. We also neglect the contribution of the gain/loss terms to the momentum source. To begin, we use the electron drift-diffusion equation (2.6) to rewrite the source as

$$S_i = \frac{kT_e}{m_i}\nabla n_i + \frac{en_i}{m_i}E - \nu_{in} n_i u_i - \frac{1}{m_i}(m_e \nu_{en} n_e u_e + en_e E + kT_e \nabla n_e) \tag{3.19}$$

$$= \frac{kT_e}{m_i}\nabla(n_i - n_e) + \frac{e}{m_i}E(n_i - n_e) - \nu_{in} n_i u_i - \frac{m_e}{m_i}\nu_{en} n_e u_e. \tag{3.20}$$

To facilitate the estimation of the relative sizes of these terms, we apply several scalings. Let $n_0$ denote the number density of the neutral background, and let $\sigma_i$ denote the ion collision cross section corresponding to $\nu_{in}$, i.e.,

$$\nu_{in} = \sigma_i n_0 \left(\frac{kT_i}{m_i}\right)^{1/2}. \tag{3.21}$$

Let

$$\phi' \equiv \frac{e\phi}{kT_e}, \tag{3.22}$$

$$u_0 \equiv \left(\frac{kT_e}{m_i}\right)^{1/2}, \tag{3.23}$$

$$u_i' \equiv \frac{u_i}{u_0}, \quad u_e' \equiv \frac{u_e}{u_0}, \tag{3.24}$$

$$n_i' \equiv \frac{n_i}{n_0}, \quad n_e' \equiv \frac{n_e}{n_0}, \tag{3.25}$$

$$\lambda \equiv \frac{1}{n_0\sigma_i}, \tag{3.26}$$

$$x' \equiv \frac{x}{\lambda}, \tag{3.27}$$

$$t' \equiv t\frac{u_0}{\lambda}. \tag{3.28}$$

The application of (3.22)–(3.28) yields

$$n_i'\frac{Du_i'}{Dt'} + \left(1+\frac{T_i}{T_e}\right)\nabla' n_i' = \nabla'(n_i' - n_e') + (n_e' - n_i')\nabla'\phi' - \frac{m_e}{m_i}\nu_{en}' n_e' u_e' - \nu_{in}' n_i' u_i', \tag{3.29}$$

where $\nabla'$ denotes the gradient with respect to the scaled spatial variable $x'$ and the $\nu_{xn}'$ are the scaled collision frequencies. Using (3.21), we have in particular that

$$\nu_{in}' \equiv \nu_{in}\frac{\lambda}{u_0} = \left(\frac{T_i}{T_e}\right)^{1/2} \tag{3.30}$$

and, using a similar expression for the electron collision frequency [12],

$$\nu_{en}' \equiv \nu_{en}\frac{\lambda}{u_0} = \sigma_e n_0\left(\frac{kT_e}{m_e}\right)^{1/2}\frac{\lambda}{u_0} = \frac{\sigma_e}{\sigma_i}\left(\frac{m_i}{m_e}\right)^{1/2}. \tag{3.31}$$

Hence, we have

$$\begin{aligned} &n_i'\frac{Du_i'}{Dt'} + \left(1+\frac{T_i}{T_e}\right)\nabla' n_i' \\ &\quad = \nabla'(n_i' - n_e') + (n_e' - n_i')\nabla'\phi' - \frac{\sigma_e}{\sigma_i}\left(\frac{m_e}{m_i}\right)^{1/2} n_e' u_e' - \left(\frac{T_i}{T_e}\right)^{1/2} n_i' u_i'. \end{aligned} \tag{3.32}$$

Although the neutral collision frequencies for the ions and electrons typically differ by a couple orders of magnitude, this is primarily due to the relative difference in their thermal speeds rather than their collision cross sections $\sigma_e$ and $\sigma_i$ (e.g., see Table II), which we therefore regard as comparable in this analysis.

The scaling (3.22)–(3.28) has effectively normalized wave velocities in (3.32) since the scaled sound speed $\sqrt{1+T_i/T_e}$ is approximately unity, assuming $T_e \gg T_i$. To see that the right-hand side does not contain small (relative to unity) time scales, we next show that the spatially differentiated (i.e., the first and second) terms in the right-hand side of (3.32)

**TABLE II**
**Sample Physical Data**

| | |
|---|---|
| Electrons | |
| $m_e$ | $9.1 \times 10^{-31}$ kg |
| $kT_e$ | $3.2 \times 10^{-19}$ joules |
| $\sigma_e$ | $1.2 \times 10^{-19}$ m$^2$ |
| Ions (Argon) | |
| $m_i$ | $6.6 \times 10^{-26}$ kg |
| $kT_i$ | $8.0 \times 10^{-21}$ joules |
| $\sigma_i$ | $8.0 \times 10^{-19}$ m$^2$ |
| Neutral background | |
| $n_0$ | $10^{21}$ m$^{-3}$ |

are in fact small and slowly varying, and that the third and fourth terms are bounded damping terms.

Differentiation of Poisson's equation (2.11) with respect to time and use of the ion and electron continuity equations yields

$$\frac{\epsilon_0}{e}\frac{\partial}{\partial t}\nabla^2\phi = -\nabla\cdot(n_e u_e) + \nabla\cdot(n_i u_i). \tag{3.33}$$

Inserting the drift-diffusion electron flux and applying the scalings (3.22)–(3.28), we obtain

$$\epsilon\frac{\partial}{\partial t'}\nabla'^2\phi' = -\nabla'\cdot\left(\frac{n_e'}{\nu_{en}'}\nabla'\phi' - \frac{1}{\nu_{en}'}\nabla' n_e'\right) + \frac{m_e}{m_i}\nabla'\cdot(n_i' u_i'), \tag{3.34}$$

where

$$\epsilon \equiv \frac{m_e\epsilon_0}{e^2 n_0}\frac{u_0^2}{\lambda^2} \tag{3.35}$$

is the squared reciprocal of the scaled plasma frequency computed with the neutral density. Taking $\epsilon$ as an asymptotic parameter tending to zero ($\epsilon = 9.8 \times 10^{-13}$ for the data in Table II), we expand $\phi'$ in $\epsilon$ as

$$\phi' = \sum_{i=0}^{\infty}\epsilon^i\phi_i' \tag{3.36}$$

and substitute into (3.34). Equating the coefficients of like powers of $\epsilon$, the zeroth-order terms yield that

$$\frac{1}{\nu_{en}'}\nabla'\cdot(n_e'\nabla'\phi_0' - \nabla' n_e') = \frac{m_e}{m_i}\nabla'\cdot(n_i' u_i'), \tag{3.37}$$

and the first-order relation is

$$\frac{\partial}{\partial t'}\nabla'^2\phi_0' = -\frac{1}{\nu_{en}'}\nabla'\cdot(n_e'\nabla'\phi_1'). \tag{3.38}$$

Using the scaled Poisson equation, we therefore have that

$$n_e' - n_i' = \epsilon \frac{m_i}{m_e} \nabla'^2 \phi' = O\left(\epsilon \frac{m_i}{m_e}\right) \quad \text{as } \epsilon \to 0 \tag{3.39}$$

and, using (3.31) and (3.38),

$$\begin{aligned} \frac{\partial}{\partial t'}(n_e' - n_i') &= \epsilon \frac{m_i}{m_e} \frac{\partial}{\partial t'} \nabla'^2 \phi_0' + O\left(\epsilon^2 \frac{m_i}{m_e}\right) && \text{as } \epsilon \to 0 \\ &= -\epsilon \frac{m_i}{m_e \nu_{en}'} \nabla' \cdot (n_e' \nabla' \phi_1') + O\left(\epsilon^2 \frac{m_i}{m_e}\right) && \text{as } \epsilon \to 0 \qquad (3.40) \\ &= O\left(\epsilon \left(\frac{m_i}{m_e}\right)^{1/2}\right) && \text{as } \epsilon \to 0. \end{aligned}$$

This implies that the first and second terms in the right-hand side of (3.29) are small, as well as their rate of change.

From (3.37), we obtain that the divergence of the ion and electron fluxes are comparable to leading order in $\epsilon$. In one spatial dimension, it then follows by integration that the fluxes themselves are comparable. This implies that, like the fourth term, the third term in the right-hand side of (3.29) is simply a nondifferentiated damping term. More generally, we may only deduce the compatibility of fluxes integrated over the boundaries of spatial subregions. There is nothing to prevent, for example, a situation in which the ion flux has components only in the $x$-direction and the electron flux has components solely in the $y$-direction. In any case, since

$$\begin{aligned} \left(\frac{m_e}{m_i}\right)^{1/2} n_e' u_e' &= \left(\frac{m_i}{m_e}\right)^{1/2} \frac{1}{\nu_{en}'} (n_e' \nabla' \phi_0' - \nabla' n_e') + O(\epsilon) \quad \text{as } \epsilon \to 0 \qquad (3.41) \\ &= O(1) \qquad \text{as } \epsilon \to 0, \qquad (3.42) \end{aligned}$$

the electron flux term in the right-hand side of (3.29) is, at worst, a bounded, nondifferentiated source term.

The scaling analysis employed above has another important implication for numerical discretization. Consider the temporal discretization of (3.34) (dropping primes)

$$\epsilon \nabla^2 \left(\frac{\phi^{n+1} - \phi^n}{\Delta t}\right) = -\nabla \cdot \left(\frac{n_e}{\nu_{en}} \nabla(\alpha \phi^n + (1-\alpha)\phi^{n+1}) - \frac{1}{\nu_{en}} \nabla n_e\right) + \frac{m_e}{m_i} \nabla \cdot (n_i u_i), \tag{3.43}$$

where $\phi^n$ and $\phi^{n+1}$ are the old and new time potentials, respectively, and $\Delta t$ is the time step. The parameter $\alpha$ is a to-be-determined weight, and the remaining discretizations are not important. Rearranging terms, we obtain

$$\nabla \cdot \left[\left(1 + \frac{(1-\alpha)\Delta t n_e}{\epsilon \nu_{en}}\right) \nabla \phi^{n+1}\right] = \nabla \cdot \left[\left(1 - \frac{\alpha \Delta t n_e}{\epsilon \nu_{en}}\right) \nabla \phi^n\right] + \text{other terms}. \tag{3.44}$$

Since stability requires that

$$\alpha \Delta t < \frac{\epsilon \nu_{en}}{n_e} = O\left(\epsilon \left(\frac{m_i}{m_e}\right)^{1/2}\right) \quad \text{as } \epsilon \to 0, \tag{3.45}$$

a severe timestep restriction results unless $\alpha = O(\epsilon\sqrt{m_i/m_e})$. In other words, the potential in the electron drift flux term must be treated implicitly. The necessity for maintaining a tight coupling of the electron drift flux and the evolution of Poisson's equation to avoid *dielectric relaxation* timestep limitations has also been recognized in other numerical approaches [1, 9, 13].

### 3.2. *Time-Split Integration Algorithm*

We employ a conservative spatial differencing that begins with the cell averaging of each of the continuous equations on an underlying uniform grid. The divergence operator then becomes a surface integral operator,

$$\nabla \cdot F \equiv \frac{1}{\Delta x \Delta y} \oint F \cdot dS.$$

For the remainder of this section the dependent variables will represent cell averages, and the usual differential notation for the divergence operator (with the above interpretation) is retained for convenience.

Assume that we have known values for all quantities at time $t^n$ and that we wish to integrate (2.5)–(2.11) to a new time $t^{n+1} = t^n + \Delta t$. The integration is split into five main steps:

1. Apply a second-order Godunov method to integrate the ion equations using lagged (i.e., evaluated at time $t^n$) sources.
2. Use a second-order Godunov method to predict time-centered electron densities at cell edges, based on the lagged electron drift velocity and diffusive flux. Implicitly solve the electron continuity equation for a prediction of the cell-centered electron density at time $t^{n+1}$ and use it to compute an updated diffusive flux.
3. Solve a modified Poisson equation for the potential at the new time $t^{n+1}$. Use the resulting new electric field to update the electron density and flux.
4. Using the new electric field, electron density, and electron flux, combine a second-order Godunov advection with an implicit treatment of the diffusive terms to integrate the electron internal energy equation.
5. Use the new time data computed in the preceding steps to compute more accurate ion source terms and update the ion density and fluxes at time $t^{n+1}$.

We describe each of these five steps in detail in Subsections 3.2.1 through 3.2.5, respectively. The selection of the timestep $\Delta t$ is described in Section 3.4.

*3.2.1. Step 1 (Ion equation integration).* To perform the ion integration, we notice that the system of Eqs. (2.1)–(2.4) for each ion species can be written as a single vector equation

$$\frac{\partial U}{\partial t} + \frac{\partial}{\partial x} F(U) + \frac{\partial}{\partial y} G(U) = H(U, E), \tag{3.46}$$

where we have the definitions:

$$U \equiv \begin{bmatrix} n_i \\ \Gamma_x \\ \Gamma_y \\ \frac{1}{2} u_i \cdot u_i + \mathcal{E}_i/m_i \end{bmatrix}, \quad \Gamma_x \equiv n_i u_{ix}, \quad \Gamma_y \equiv n_i u_{iy}, \tag{3.47}$$

$$c^2 \equiv \frac{\gamma_i k T_i + k T_e}{m_i}, \tag{3.48}$$

$$F(U) \equiv \begin{bmatrix} \Gamma_x \\ \frac{\Gamma_x^2}{n_i} + c^2 n_i \\ \frac{\Gamma_x \Gamma_y}{n_i} \\ \left(\frac{1}{2} u_i \cdot u_i + \mathcal{E}_i / m_i + c^2\right) \Gamma_x \end{bmatrix}, \quad G(U) \equiv \begin{bmatrix} \Gamma_y \\ \frac{\Gamma_x \Gamma_y}{n_i} \\ \frac{\Gamma_y^2}{n_i} + c^2 n_i \\ \left(\frac{1}{2} u_i \cdot u_i + \mathcal{E}_i / m_i + c^2\right) \Gamma_y \end{bmatrix}, \tag{3.49}$$

$$H(U, E) \equiv \frac{1}{m_i} \begin{bmatrix} S_0 \\ k T_e \frac{\partial n_i}{\partial x} + q_i n_i E_x + S_{1x} \\ k T_e \frac{\partial n_i}{\partial y} + q_i n_i E_y + S_{1y} \\ \nabla \cdot (n_i k T_e u_i) + q_i n_i u_i \cdot E + S_2 \end{bmatrix}, \tag{3.50}$$

where $S_0$, $S_1$, and $S_2$ denote the collisional and gain/loss terms in the right-hand sides of (2.1)–(2.3). As described in Section 3.1, the above system is modified for electronegative plasmas as

$$c^2 \equiv \begin{cases} (\gamma_i k T_i + \beta k T_e)/m_i, & \text{if } q_i > 0, \\ k T_i / m_i, & \text{if } q_i < 0, \end{cases} \tag{3.51}$$

$$H(U, E) \equiv \frac{1}{m_i} \begin{bmatrix} S_0 \\ \beta k T_e \frac{\partial n_i}{\partial x} + q_i n_i E_x + S_{1x} \\ \beta k T_e \frac{\partial n_i}{\partial y} + q_i n_i E_y + S_{1y} \\ \nabla \cdot (n_i \beta k T_e u_i) + q_i n_i u_i \cdot E + S_2 \end{bmatrix}, \quad \text{if } q_i > 0, \tag{3.52}$$

or

$$H(U, E) \equiv \frac{1}{m_i} \begin{bmatrix} S_0 \\ q_i n_i E_x + S_{1x} \\ q_i n_i E_y + S_{1y} \\ q_i n_i u_i \cdot E + S_2 \end{bmatrix}, \quad \text{if } q_i < 0, \tag{3.53}$$

where $\beta$ is defined by (3.18). We use a second-order, unsplit Godunov method [3] to solve this system.

THE GODUNOV PROCEDURE. To cell average (3.46) we apply to each term

$$\frac{1}{\Delta t \Delta x \Delta y} \int_{t^n}^{t^{n+1}} dt \int_{x_{i-1/2}}^{x_{i+1/2}} dx \int_{y_{j-1/2}}^{y_{j+1/2}} dy. \tag{3.54}$$

The first term in (3.46) becomes

$$\frac{U_{i,j}^{n+1} - U_{i,j}^n}{\Delta t},$$

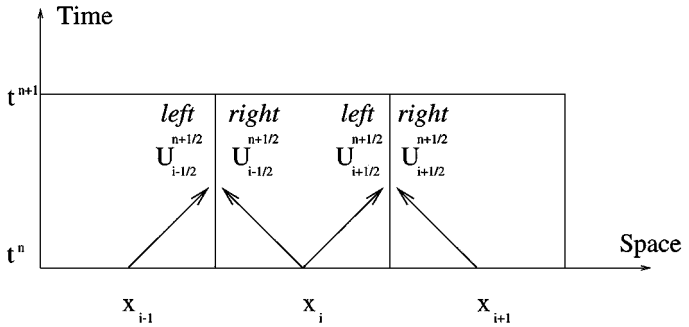


**FIG. 1.** Calculation of left and right states for Riemann problems for edges normal to the $x$ direction. Arrows indicate position for state predictions relative to base of Taylor expansion.

where $U^n_{i,j}$ is a vector quantity representing the average value in cell $(i, j)$ at time $t^n$, of the pointwise vector quantity $u$.

The second and third terms represent time-averaged flux values through cell faces within a timestep. These flux values are obtained by evaluating the flux functions $F(U)$ and $G(U)$ using the solution of local Riemann problems at the cell interfaces (as in [10]). The states used to calculate the Riemann solution are detailed below, but it is important to point out that, rather than using cell-centered values from the previous timestep for these states, we use Taylor series expansions in time and space about the cell-centered values for higher accuracy. These edge state values are depicted in Fig. 1 for the case of edges normal to the $x$ direction. Using these states increases the spatial and temporal accuracy to second-order (at least in the case of linear advection). If we represent these Riemann solutions by $\tilde{U}^n_{i\pm1/2,j}$ and $\tilde{U}^n_{i,j\pm1/2}$, the second and third terms can be written as

$$\frac{1}{\Delta x}\left[F\left(\tilde{U}^n_{i+1/2,j}\right) - F\left(\tilde{U}^n_{i-1/2,j}\right)\right],$$
$$\frac{1}{\Delta y}\left[G\left(\tilde{U}^n_{i,j+1/2}\right) - G\left(\tilde{U}^n_{i,j-1/2}\right)\right].$$

The discrete source term is calculated in two steps. First, the values of the state variables at $t^n$ are used to calculate a provisional update $U^{*n+1}_{i,j}$ at time $t^{n+1}$. The update is recalculated using this value for the source term $H(U^{*n+1}_{i,j}, E^{n+1})$. In this way, a more accurate description of the source evolution during the step is obtained. This gives for the fourth term

$$\frac{1}{2}\left[H\left(U^n_{i,j}, E^n\right) + H\left(U^{*n+1}_{i,j}, E^{n+1}\right)\right].$$

Rearranging gives the update scheme for the cell averages,

$$U^{n+1}_{i,j} = U^n_{i,j} - \frac{\Delta t}{\Delta x}\left[F\left(\tilde{U}^n_{i+1/2,j}\right) - F\left(\tilde{U}^n_{i-1/2,j}\right)\right] - \frac{\Delta t}{\Delta y}\left[G\left(\tilde{U}^n_{i,j+1/2}\right) - G\left(\tilde{U}^n_{i,j-1/2}\right)\right]$$
$$+ \frac{\Delta t}{2}\left[H\left(U^n_{i,j}, E^n\right) + H\left(U^{*n+1}_{i,j}, E^{n+1}\right)\right]. \tag{3.55}$$

THE RIEMANN SOLVER. Central to the Godunov algorithm is the solution of Riemann problems at cell edges. Because the system of equations describing each ion species is essentially the Euler equations of ordinary gas dynamics with a modified sound speed (due

to the rearrangement (3.13)) and source terms, approximate Riemann problem solutions can be obtained in the same manner as for a neutral gas [10].

The Riemann solver returns a solution at a cell edge, given the states on both sides. The solver decomposes the jump into wave components and determines from the wave speeds the solution at the interface during the timestep. This Riemann solution is then used to evaluate the flux functions $F$ and $G$ in (3.46). The solver is locally one-dimensional in that the transverse behavior is included only as a source term in the calculation of the left and right states. The term unsplit is in contrast to methods using Strang splitting [14]. Rather than alternating between directions on subsequent steps, as in a split method, each edge (normal to $x$ or $y$) is treated independently and on an equal footing during each step.

HALF-STEP PREDICTIONS. In order to calculate the edge fluxes, a Riemann problem must be solved at each cell edge. If lagged cell-centered data is used as input to the Riemann solver, the method is first order (in the case of linear advection). Higher order interpolation in space alone can be used. However, this requires twice as many Riemann solves for comparable accuracy [10].

The approach we have chosen is to Taylor-expand in space and time about the cell-centered value at $t^n$ to get a better approximation to the edge states at $t^{n+1/2}$. This allows the Riemann solves to be done, operationally, as in the first-order case, but with second-order accuracy (this can be shown analytically for the case of linear advection and computationally for Burgers' equation). The difference is that we are using more accurate (spatially and temporally) values for the left and right states in the Riemann solve.

So, the left and right state values for the edge-bordering cells $(i, j)$ and $(i+1, j)$, depicted in Fig. 1, and the bottom and top states for the edge bordering cells $(i, j)$ and $(i, j+1)$ will be

$$
\begin{aligned}
U^{n+1/2}_{i+1/2,j}\big|^L &= U^n_{i,j} + \frac{\Delta t}{2}\frac{\partial U}{\partial t}\bigg|^n_{i,j} + \frac{\Delta x}{2}\frac{\partial U}{\partial x}\bigg|^n_{i,j},\\
U^{n+1/2}_{i+1/2,j}\big|^R &= U^n_{i+1,j} + \frac{\Delta t}{2}\frac{\partial U}{\partial t}\bigg|^n_{i+1,j} - \frac{\Delta x}{2}\frac{\partial U}{\partial x}\bigg|^n_{i+1,j},\\
U^{n+1/2}_{i,j+1/2}\big|^B &= U^n_{i,j} + \frac{\Delta t}{2}\frac{\partial U}{\partial t}\bigg|^n_{i,j} + \frac{\Delta y}{2}\frac{\partial U}{\partial y}\bigg|^n_{i,j},\\
U^{n+1/2}_{i,j+1/2}\big|^T &= U^n_{i,j+1} + \frac{\Delta t}{2}\frac{\partial U}{\partial t}\bigg|^n_{i,j+1} - \frac{\Delta y}{2}\frac{\partial U}{\partial y}\bigg|^n_{i,j+1}.
\end{aligned}
\tag{3.56}
$$

The time derivatives are then replaced with spatial derivatives using the conservation law (3.46) in quasi-linear form to obtain

$$
\begin{aligned}
U^{n+1/2}_{i+1/2,j}\big|^L &= U^n_{i,j} + \frac{\Delta x}{2}\frac{\partial U}{\partial x}\left[I - \frac{\Delta t}{\Delta x}\partial F\right]\bigg|^n_{i,j} - \frac{\Delta t}{2}G_y\bigg|^n_{i,j} + \frac{\Delta t}{2}H\bigg|^n_{i,j},\\
U^{n+1/2}_{i+1/2,j}\big|^R &= U^n_{i+1,j} - \frac{\Delta x}{2}\frac{\partial U}{\partial x}\left[I + \frac{\Delta t}{\Delta x}\partial F\right]\bigg|^n_{i+1,j} - \frac{\Delta t}{2}G_y\bigg|^n_{i+1,j} + \frac{\Delta t}{2}H\bigg|^n_{i+1,j},\\
U^{n+1/2}_{i,j+1/2}\big|^B &= U^n_{i,j} + \frac{\Delta y}{2}\frac{\partial U}{\partial y}\left[I - \frac{\Delta t}{\Delta y}\partial G\right]\bigg|^n_{i,j} - \frac{\Delta t}{2}F_x\bigg|^n_{i,j} + \frac{\Delta t}{2}H\bigg|^n_{i,j},\\
U^{n+1/2}_{i,j+1/2}\big|^T &= U^n_{i,j+1} - \frac{\Delta y}{2}\frac{\partial U}{\partial y}\left[I + \frac{\Delta t}{\Delta y}\partial G\right]\bigg|^n_{i,j+1} - \frac{\Delta t}{2}F_x\bigg|^n_{i,j+1} + \frac{\Delta t}{2}H\bigg|^n_{i,j+1},
\end{aligned}
\tag{3.57}
$$

where $\partial F$ and $\partial G$ are the Jacobians of the flux functions $F$ and $G$, respectively.

SLOPE LIMITING AND CHARACTERISTIC PROJECTION. We further modify the state predictions (3.57) to enhance stability. We first want to use slope limiting to prevent oscillations that could feed into nonlinear instabilities. Second, we wish to take advantage of local characteristic information and remove portions of the Taylor series expansion that do not come from the "upwind" direction. The first of these objectives is accomplished through the use of the van Leer slope-limiting operator, denoted $SL$. The upwinding is done with two projection operators $P_+$ and $P_-$ as described in [5].

Including the slope limiting and characteristic projection operators, we have our final representation of the left/right and top/bottom state values used for the Riemann solution,

$$
\begin{aligned}
U^{n+1/2}_{i+1/2,j}\big|^L &= U^n_{i,j} + \frac{\Delta x}{2} P_+ \left\{ SL\left(\frac{\partial U}{\partial x}\right)\left[I - \frac{\Delta t}{\Delta x}\partial F\right]\right\}\Big|^n_{i,j} - \frac{\Delta t}{2} G_y\Big|^n_{i,j} + \frac{\Delta t}{2} H\Big|^n_{i,j},\\
U^{n+1/2}_{i+1/2,j}\big|^R &= U^n_{i+1,j} - \frac{\Delta x}{2} P_- \left\{ SL\left(\frac{\partial U}{\partial x}\right)\left[I + \frac{\Delta t}{\Delta x}\partial F\right]\right\}\Big|^n_{i+1,j}\\
&\quad - \frac{\Delta t}{2} G_y\Big|^n_{i+1,j} + \frac{\Delta t}{2} H\Big|^n_{i+1,j},\\
U^{n+1/2}_{i,j+1/2}\big|^B &= U^n_{i,j} + \frac{\Delta y}{2} P_+ \left\{ SL\left(\frac{\partial U}{\partial y}\right)\left[I - \frac{\Delta t}{\Delta y}\partial G\right]\right\}\Big|^n_{i,j} - \frac{\Delta t}{2} F_x\Big|^n_{i,j} + \frac{\Delta t}{2} H\Big|^n_{i,j},\\
U^{n+1/2}_{i,j+1/2}\big|^T &= U^n_{i,j+1} - \frac{\Delta y}{2} P_- \left\{ SL\left(\frac{\partial U}{\partial y}\right)\left[I + \frac{\Delta t}{\Delta y}\partial G\right]\right\}\Big|^n_{i,j+1}\\
&\quad - \frac{\Delta t}{2} F_x\Big|^n_{i,j+1} + \frac{\Delta t}{2} H\Big|^n_{i,j+1}.
\end{aligned}
\tag{3.58}
$$

TWO-PASS FLUX CALCULATION. To calculate the state predictions (3.58), the cell-centered transverse fluxes must be known. For example, the prediction of the left state requires $G_y|^n_{i,j}$. To approximate these transverse flux terms, a two-pass scheme is used. In the first pass, the transverse flux terms are approximated by considering a set of homogeneous equations. We calculate the fluxes associated with the conservation laws,

$$
\begin{aligned}
\frac{\partial U}{\partial t} + \frac{\partial}{\partial x} F(U) = 0,\\
\frac{\partial U}{\partial t} + \frac{\partial}{\partial y} G(U) = 0.
\end{aligned}
$$

We will then be able to approximate $G_y|^n_{i,j}$ and $F_x|^n_{i,j}$ as

$$
\begin{aligned}
F_x|^n_{i,j} &\approx \frac{1}{\Delta x}\left(F\left(\tilde{U}^n_{i+1/2,j}\right) - F\left(\tilde{U}^n_{i-1/2,j}\right)\right),\\
G_y|^n_{i,j} &\approx \frac{1}{\Delta y}\left(G\left(\tilde{U}^n_{i,j+1/2}\right) - G\left(\tilde{U}^n_{i,j-1/2}\right)\right).
\end{aligned}
$$

With these transverse values, we can then calculate the state predictions in (3.58) in a second pass.

*3.2.2. Step 2 (Electron diffusive flux calculation).* To begin the electron advance, we substitute (2.6) into (2.5) to obtain

$$\frac{\partial n_e}{\partial t} = -\nabla \cdot (n_e \bar{u}_e) + \nabla \cdot \eta \nabla (n_e k T_e) + \sum_j R_{ej}, \tag{3.59}$$

where $\bar{u}_e \equiv -\mu E$ is the electron drift velocity. We calculate a slope-limited, Taylor-series prediction of the edge electron density $n_e^{n+1/2}$ at $t^{n+1/2} \equiv (t^n + t^{n+1})/2$ upwinded relative to the lagged drift velocity $\bar{u}_e^n$. Specifically, on cell edges parallel to the $y$-axis,

$$n_e|^{n+1/2}_{i+1/2,\,j} = \begin{cases} n_e|^n_{i,\,j} + \frac{\Delta t}{2}\frac{\partial n_e}{\partial t}\big|^n_{i,\,j} + \frac{\Delta x}{2}\frac{\partial n_e}{\partial x}\big|^n_{i,\,j} & \text{for } \bar{u}_e|^n_{i+1/2,\,j} > 0, \\ n_e|^n_{i+1,\,j} + \frac{\Delta t}{2}\frac{\partial n_e}{\partial t}\big|^n_{i+1,\,j} - \frac{\Delta x}{2}\frac{\partial n_e}{\partial x}\big|^n_{i+1,\,j} & \text{for } \bar{u}_e|^n_{i+1/2,\,j} \le 0, \end{cases} \tag{3.60}$$

and similarly for the cell edges parallel to the $x$-axis. As for the ion equations, the temporal derivatives in (3.60) are replaced using the quasi-linear form of (3.59) and the spatial derivative $\partial n_e/\partial x$, which is slope limited.

Using the half-step prediction $n_e^{n+1/2}$ in the electron drift flux term, we then discretize (3.59) as

$$\frac{\hat{n}_e^{n+1} - n_e^n}{\Delta t} = -\nabla \cdot \left(n_e^{n+1/2} \bar{u}_e^n\right) + \nabla \cdot \eta^n \nabla \left(\hat{n}_e^{n+1} k T_e^n\right) + \sum_j R_{ej}^n. \tag{3.61}$$

Collecting terms involving $\hat{n}_e^{n+1}$ on the left-hand side yields a symmetric, positive definite linear system that can be solved for this quantity. The density $\hat{n}_e^{n+1}$ is merely a prediction of the electron density at time $t^{n+1}$ that we employ to compute the electron diffusive flux

$$\Gamma_{\text{diff}}^{n+1} \equiv -\eta^n \nabla \left(\hat{n}_e^{n+1} k T_e^n\right). \tag{3.62}$$

*3.2.3. Step 3 (Coupled potential and electron integration).* Using the electron diffusive flux $\Gamma_{\text{diff}}^{n+1}$ and the electron densities $n_e^{n+1/2}$, we are ready to advance the potential and compute the final electron density at time $t^{n+1}$. As shown at the end of Section 3.1, the electron drift flux represents a stiff term that must be treated implicitly. As in (3.43), we difference (2.11) in time to obtain

$$\frac{\epsilon_0}{e}\frac{\nabla^2 \phi^{n+1} - \nabla^2 \phi^n}{\Delta t} = \frac{n_e^{n+1} - n_e^n}{\Delta t} - \sum_i \frac{q_i}{e}\frac{n_i^{n+1} - n_i^n}{\Delta t}; \tag{3.63}$$

then we use the continuity equation to replace the first term on the right-hand side by

$$\frac{n_e^{n+1} - n_e^n}{\Delta t} = -\nabla \cdot \Gamma_e^{n+1} + \sum_j R_{ej}^n, \tag{3.64}$$

where

$$\Gamma_e^{n+1} \equiv \mu^n n_e^{n+1/2} \nabla \phi^{n+1} + \Gamma_{\text{diff}}^{n+1}. \tag{3.65}$$

Using the discrete ion continuity equations in the second term on the right-hand side of (3.63), collecting all terms involving $\phi^{n+1}$ on the left-hand side, and using Poisson's equation

at the old time, we obtain

$$\nabla\cdot\left[\left(\frac{\epsilon_0}{e}+\mu^n\Delta t n_e^{n+1/2}\right)\nabla\phi^{n+1}\right]=n_e^n-\sum_i\frac{q_i}{e}n_i^n+\Delta t\nabla\cdot\left(\sum_i\frac{q_i}{e}(n_iu_i)^{n+1/2}-\Gamma_{\text{diff}}^{n+1}\right). \tag{3.66}$$

Here, we have also used the fact that the gain/loss terms $R_{ej}^n$, $R_{ij}^n$ yield zero net charge, i.e.,

$$\sum_j\left(q_eR_{ej}^n+\sum_i q_iR_{ij}^n\right)=0. \tag{3.67}$$

Equation (3.66), together with boundary conditions, is a symmetric linear system that can be solved for $\phi^{n+1}$. The final electron flux is then computed from (3.65), $n_e^{n+1}$ is obtained from (3.64), and the new field is given by

$$E^{n+1}\equiv-\nabla\phi^{n+1}. \tag{3.68}$$

*3.2.4. Step 4 (Electron internal energy equation integration).* We discretize (2.7) as

$$\begin{aligned}&\frac{3}{2}\frac{n_e^{n+1}kT_e^{n+1}-n_e^nkT_e^n}{\Delta t}+\nabla\cdot\left(\frac{5}{2}\Gamma_e^{n+1}kT_e^{n+1/2}\right)\\&\quad=-e\Gamma_e^{n+1}\cdot E^{n+1}+\frac{5}{2}\nabla\cdot\left(\eta^n n_e^{n+1/2}kT_e^{n+1/2}\nabla kT_e^{n+1}\right)\\&\qquad+P_{\text{ind}}^n-\sum_j\frac{3m_e}{m_j}kT_e^n\nu_{ej}^nn_e^n+\sum_j\epsilon_{ej}^nS_{ej}^n,\end{aligned} \tag{3.69}$$

where $T_e^{n+1/2}$ is a slope-limited, Taylor-series prediction of the edge temperature at $t^{n+1/2}$ upwinded relative to the velocity $u_e^n$ (similarly to (3.60)). Collecting all terms involving $T_e^{n+1}$ on the left-hand side, we obtain, together with boundary conditions, a symmetric, positive definite linear system that can be solved for this quantity.

*3.2.5. Step 5 (Ion data update).* At this point, all that remains is the final update of the ion data. To do this, we must evaluate the source term $H(U,E)$ in Eq. (3.46). At the start of the timestep we have the data

$$U=U^n\equiv\begin{bmatrix}n_i^n\\n_i^nu_{ix}^n\\n_i^nu_{iy}^n\\\frac{1}{2}u_i^n\cdot u_i^n+\mathcal{E}_i^n/m_i\end{bmatrix},\quad E=E^n. \tag{3.70}$$

At the end of Step 3, we have provisional values for the ion data and final values for the field

$$U=\hat{U}^{n+1}\equiv\begin{bmatrix}\hat{n}_i^{n+1}\\\hat{n}_i^{n+1}\hat{u}_{ix}^{n+1}\\\hat{n}_i^{n+1}\hat{u}_{iy}^{n+1}\\\frac{1}{2}\hat{u}_i^{n+1}\cdot\hat{u}_i^{n+1}+\hat{\mathcal{E}}_i^{n+1}/m_i\end{bmatrix},\quad E=E^{n+1}. \tag{3.71}$$

We then average the source term evaluated with these two states. This is much like Heun's method [6] and is second-order accurate in time. With this source term we can calculate the new solution of the conservation law (3.46),

$$U^{n+1} = U^n - \frac{\Delta t}{\Delta x}\left[F\left(\tilde{U}_R^{n+1/2}\right) - F\left(\tilde{U}_L^{n+1/2}\right)\right] - \frac{\Delta t}{\Delta y}\left[G\left(\tilde{U}_T^{n+1/2}\right) - G\left(\tilde{U}_B^{n+1/2}\right)\right] + \frac{\Delta t}{2}[H(U^n, E^n) + H(\hat{U}^{n+1}, E^{n+1})], \tag{3.72}$$

where $\tilde{U}_R^{n+1/2}$, $\tilde{U}_L^{n+1/2}$, $\tilde{U}_T^{n+1/2}$, and $\tilde{U}_B^{n+1/2}$ are Riemann solutions used to evaluate the time-centered fluxes on the right, left, top, and bottom cell edges, respectively.

### 3.3. *Boundary Conditions*

Boundary conditions for the discrete ion equations are applied in the solution of the Riemann problems at boundary cell edges. The Riemann problem solutions give the nonlinear equivalent of upwind solutions that are used to evaluate the flux functions $F$ and $G$ in (3.46). On each interior cell edge, predictions made from both sides of the edge define the initial conditions for the Riemann problem. At cell edges on the problem boundary, we assume that for positive ion species the prediction coming from the interior of the domain is the solution to the Riemann problem. This is equivalent to assuming that the ions are flowing outward at a speed greater than the ion acoustic speed $c$ defined by (3.48), which is consistent with the well-known Bohm sheath criterion [2]. For positive ion species in an electronegative system, the use of interior predictions at the boundary is also consistent with modified Bohm criterion as described in [11] due to our inclusion of the factor $\beta$ given by (3.18) in the definition of the reduced plasma sound speed used for the hyperbolic integration. For negative ion species, we assume a zero flux boundary condition.

For Poisson's equation, Dirichlet boundary conditions are imposed on the potential $\phi$ corresponding to an applied voltage $\phi_b$ at the boundary. The applied voltage $\phi_b$ can vary spatially along the boundary and with each time step. In the simulation of ICP reactors, for example, radio-frequency (rf) biasing can be included by specifying a sinusoidally varying potential along a portion of the boundary.

The specification of boundary conditions for the discrete electron equations requires a boundary condition for the electron flux $n_e u_e$. Consider a spatial cell with an edge on the problem boundary. Let $\Gamma_b$ denote the outward normal component of $n_e u_e$ at the center of the boundary edge, and let $\phi_b$ denote the applied voltage there. Let $\phi$, $n_e$, and $T_e$ denote the potential, electron number density, and electron temperature at the cell center, respectively. Of all the electrons at the cell center, only those moving toward the boundary with kinetic energies greater than $e|\phi_b - \phi|$ can overcome the potential barrier. Using a Maxwellian distribution

$$f(w) = \left(\frac{m_e}{2\pi k T_e}\right)^{1/2} \exp\left(\frac{-m_e w^2}{2kT_e}\right), \tag{3.73}$$

we therefore propose that

$$\Gamma_b = n_e \bar{w}_e(kT_e, \phi), \tag{3.74}$$

where $\bar{w}_e$ is the average velocity of electrons reaching the boundary; i.e.,

$$\begin{aligned}\bar{w}_e(kT_e,\phi) &\equiv \int_{(2e|\phi_b-\phi|/m_e)^{1/2}}^{\infty} w f(w)\,dw \\ &= \sqrt{\frac{kT_e}{2\pi m_e}}\exp\left(-\frac{e|\phi_b-\phi|}{kT_e}\right) \\ &= \frac{\bar{v}(kT_e)}{4}\exp\left(-\frac{e|\phi_b-\phi|}{kT_e}\right),\end{aligned} \tag{3.75}$$

where $\bar{v}(kT_e)=\sqrt{8kT_e/\pi m_e}$ is the average speed for a Maxwellian distribution. Let $n_e^{n+1/2}$ again denote the Taylor-series-predicted density at the boundary. We can then require that at the problem boundary

$$n_e^{n+1/2}\bar{u}_e^{n+1} - \eta^n\nabla\left(\hat{n}_e^{n+1}kT_e^n\right) = n_e^{n+1/2}\bar{w}_e\left(kT_e^n,\phi^{n+1}\right). \tag{3.76}$$

This relation for the total flux at the boundary does not give the drift and diffusive flux components separately. Moreover, it depends upon the potential, which we are treating implicitly. This requires a modification of (3.66) to include the total electron flux, not just the drift component, on the left-hand side. Specifically, we replace (3.66) by

$$\nabla\cdot\left[\frac{\epsilon_0}{e}\nabla\phi^{n+1}+\Delta t F(\phi^{n+1})\right] = n_e^n - \sum_i \frac{q_i}{e}n_i^n + \Delta t\nabla\cdot\left(\sum_i \frac{q_i}{e}(n_iu_i)^{n+1/2} - \Gamma_{\text{diff}}^{n+1}\right), \tag{3.77}$$

where

$$F(\phi^{n+1}) \equiv \begin{cases} n_e^{n+1/2}\mu^n\nabla\phi^{n+1} & \text{on interior cell edges,} \\ n_e^{n+1/2}\bar{w}_e\left(kT_e^n,\phi^{n+1}\right) & \text{on boundary cell edges.}\end{cases} \tag{3.78}$$

Here, we assume that $\Gamma_{\text{diff}}^{n+1}=0$ on boundary cell edges, which also implies the use of homogeneous Neumann boundary conditions in the solution of the linear system in (3.61). Since the exponential nonlinearity introduced by the electron flux boundary condition (3.76) in (3.77) affects only boundary edges, (3.77) is readily solved using Newton iteration with a symmetric Jacobian.

The solution of the linear system implied by (3.69) requires a boundary condition for the total energy flux, $Q_b$. The total energy is calculated by arguments similar to those used in obtaining (3.74). A derivation for the total energy flux is shown in [11] and is given by

$$Q_b = \frac{5}{2}n_ekT_eu_e - \frac{5\eta}{2}n_ekT_e\nabla kT_e = 2kT_e\Gamma_b. \tag{3.79}$$

Although we have specified boundary conditions independently for the ion species and electrons, a coupling of boundary fluxes will occur if secondary electron emission is included. In our time-split integration algorithm, after each of the ion species has been advanced over the timestep, the inward flux of emitted electrons can be computed as a sum of terms, each of which is the product of ion flux (for the outward flowing species) times an emission coefficient depending on the ion species and boundary material. The emission flux computed in this way can then be subtracted from (3.74), which simply adds a constant term to the nonlinear problem (3.77).

As a final comment in this section, we note that the use of the electron flux boundary condition (3.74) is, in effect, a type of sheath model since it attempts to incorporate the potential drop across the sheath even if the sheath is entirely contained in the boundary cell. If, on the other hand, the sheath is resolved by the grid, the predicted boundary flux tends to the correct limit $\bar{v}(kT_e)/4$ as $|\phi - \phi_b|$ tends to zero in the exponential factor. This behavior is critical when the Cartesian grid algorithm described in this paper is used as a refinement level integrator in a locally refined grid algorithm as described in the Introduction. In particular, it is important to at least have a reasonable prediction of the electron flux during the integration of the coarser, under-resolved levels so that a smaller correction is required from the fine grid integration.

### 3.4. *Timestep Restrictions*

The implicit treatment of the electron drift flux in (3.77) allows us to exceed the very restrictive dielectric relaxation timestep limit. The dielectric relaxation time is

$$\tau_{\text{dielectric}} = \nu_{\text{en}} / \omega_{\text{p}}^2,$$

where $\nu_{\text{en}}$ is the electron neutral collision frequency and $\omega_{\text{p}}$ is the plasma frequency. For parameters such as in Table II, $\tau_{\text{dielectric}}$ can be as small as $10^{-15}$ s. The explicit nature of the electron advection in our time splitting limits us to conditional stability, however. It was our expectation that we would be limited by the Courant condition, based on the electron drift velocity, i.e.,

$$\Delta t \leq \min\left( \frac{\Delta x}{\mu |E_x|}, \frac{\Delta y}{\mu |E_y|} \right). \tag{3.80}$$

Experience with our code and a linearized stability analysis [17] have confirmed this expectation. This same analysis suggests ways in which larger timesteps may be used, but to the detriment of spatial accuracy. As will be shown in an example in the following section, the timestep restriction (3.80) is typically more severe than the corresponding Courant limits for the integration of the ion species, and it is therefore the primary control in timestep selection. The inclusion of rf-biasing at the problem-boundary can further restrict the size of timesteps in order to resolve the resulting variations.

## 4. RESULTS

In this section, we present some numerical results obtained using an implementation of the algorithm described above.

### 4.1. *Convergence Studies*

To investigate the convergence of the numerical algorithm described in Section 3, we performed a series of calculations with varying spatial grid sizes. An atomic hydrogen plasma was assumed with a constant ion and neutral temperature of 0.05 ev and neutral number density of $10^{21}$ m$^{-3}$. The ion-neutral collision cross section was $\sigma_{\text{in}} = 5.0 \times 10^{-15}$ cm$^2$, and the corresponding frequency was computed using (3.21). The ionization and electron elastic collision cross sections were obtained from analytic fits to atomic physics data [15], which resulted in the corresponding frequencies plotted in Fig. 2. The ionization energy loss coefficient was $\epsilon_{ej} = 13.565$ ev.

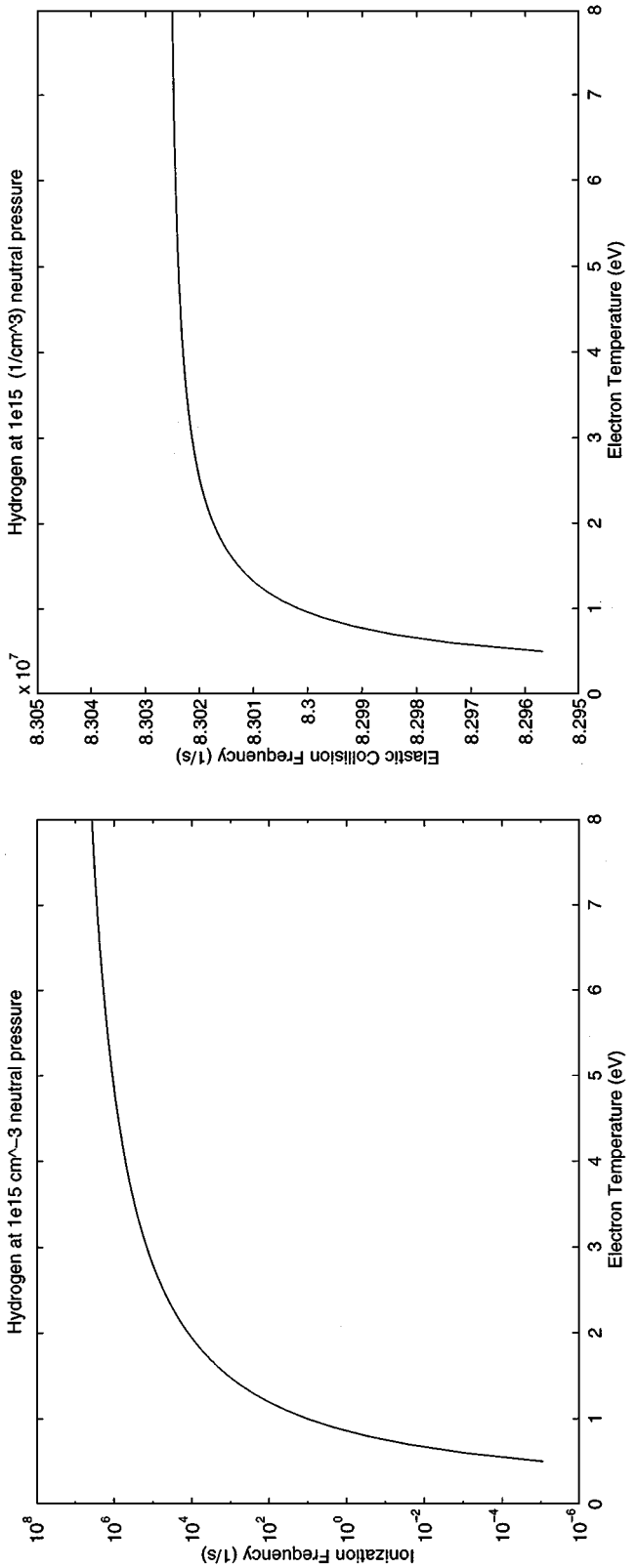


**FIG. 2.** Ionization and electron elastic collision frequencies for hydrogen plasma test problem.

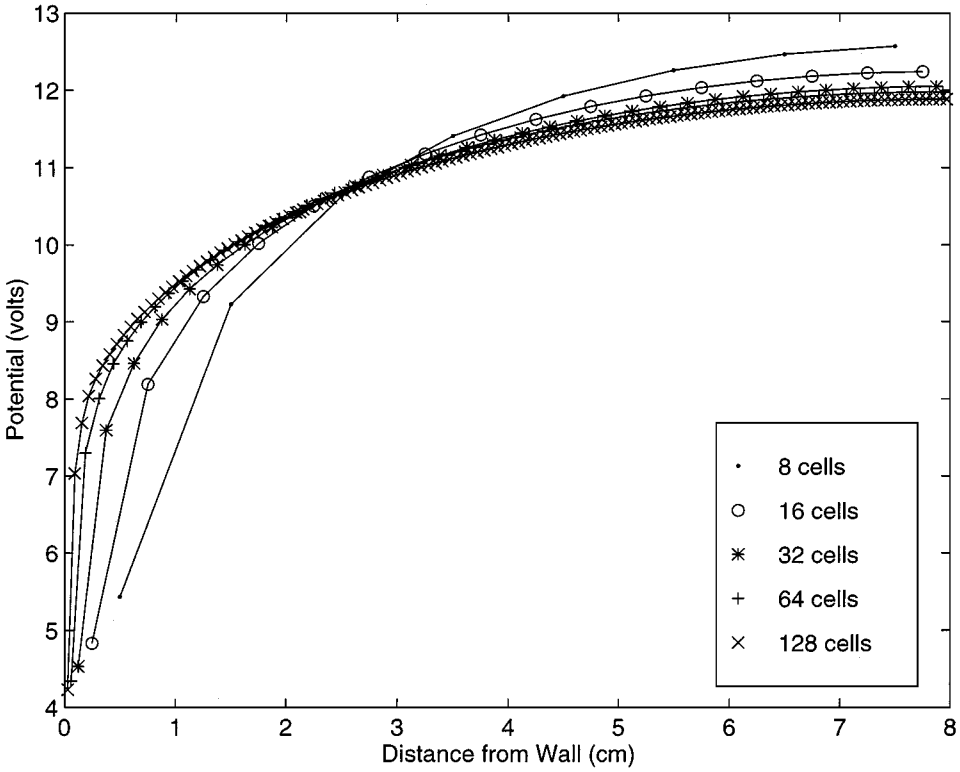


**FIG. 3.** Potential profiles (volts).

We assumed a one-dimensional spatial domain 8 cm in length with a grounded wall at the left boundary and a symmetry boundary at the right endpoint. Steady-state solutions were calculated using 8, 16, 32, 64, and 128 cells. The resulting potential, electron density, electron temperature, ion density, and ion flux are displayed in Figs. 3 through 7, respectively. Further refinements were prohibitively expensive, as is discussed in the next section. The inability to refine further makes it difficult to determine the order of the solution convergence, since we are not yet in the asymptotic regime where the higher order terms are negligible. We are, however, able to see that the solution is indeed converging. The plots suggest that the convergence is at least superlinear and we expect that it is second order.

### 4.2. *Computational Complexity*

Although the implicit treatment of the electron drift flux in (3.66) avoids the dielectric relaxation timestep restriction, we are still left with a computationally intensive problem, since many steps are required to integrate the solution to times of interest. In this section we examine the relevant time scales for a sample problem in order to better understand what we have accomplished and the limitations of our approach.

Figures 8 and 9 show results for a sample calculation at steady state. Here, an argon plasma is assumed with a constant ion and neutral temperature of 0.05 ev and a neutral density of $10^{21}$ m$^{-3}$. The ion-neutral collision cross section is $\sigma_{\text{in}} = 5.0 \times 10^{-15}$ cm$^2$, and the ionization and electron elastic collision data is obtained from [7]. The spatial domain

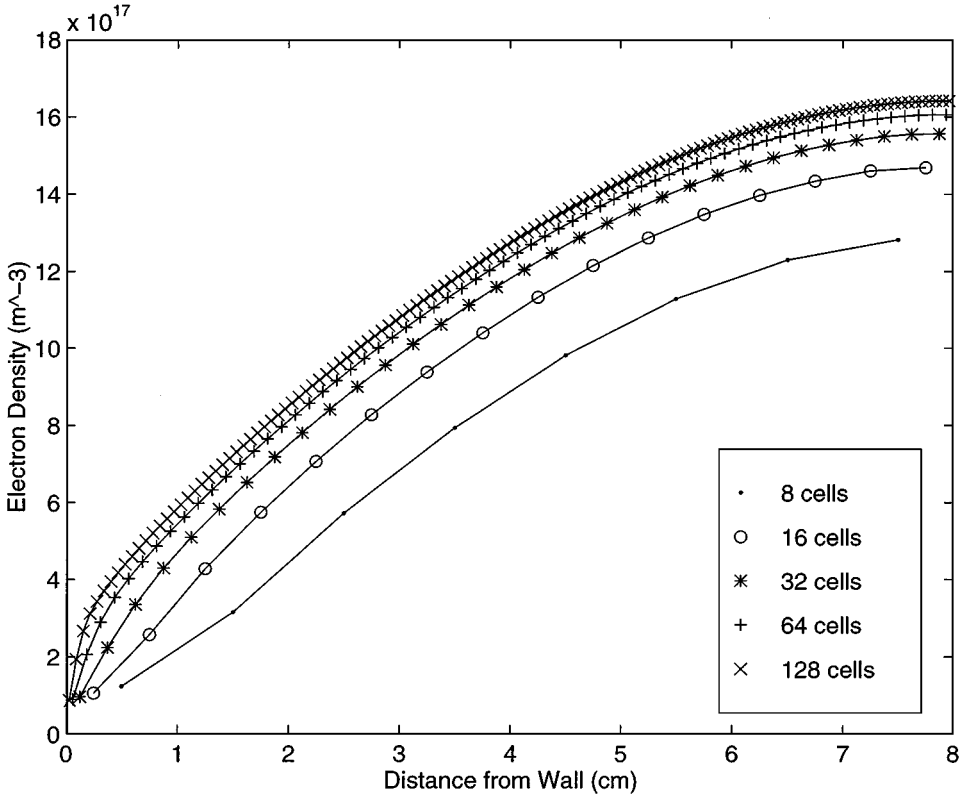


**FIG. 4.** Electron density profiles (number per cubic meter).

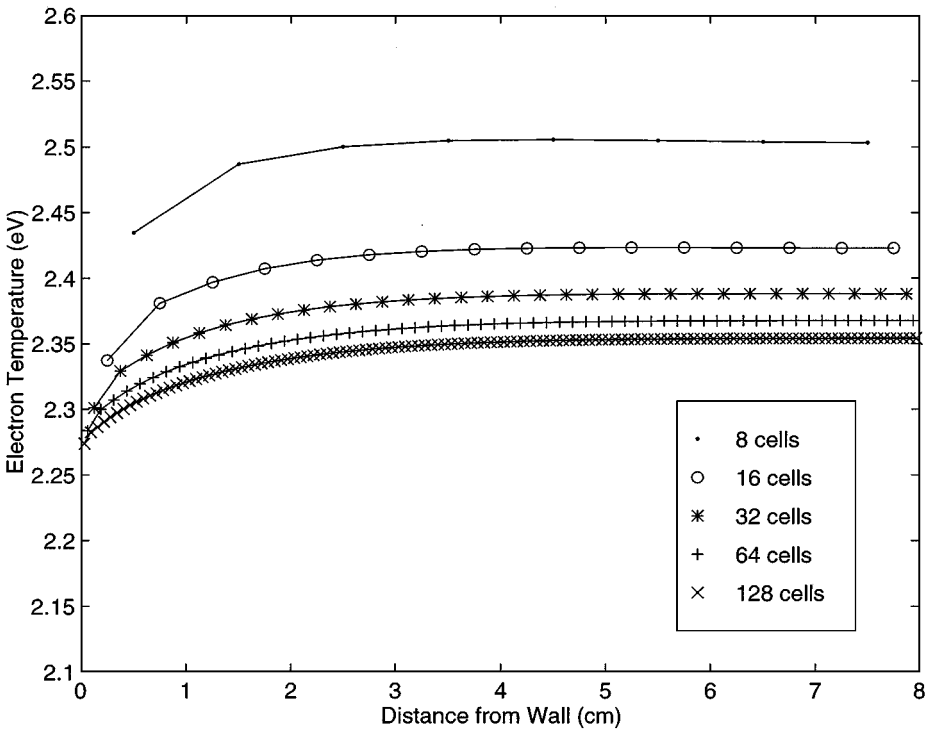


**FIG. 5.** Electron temperature profiles (electron volts).

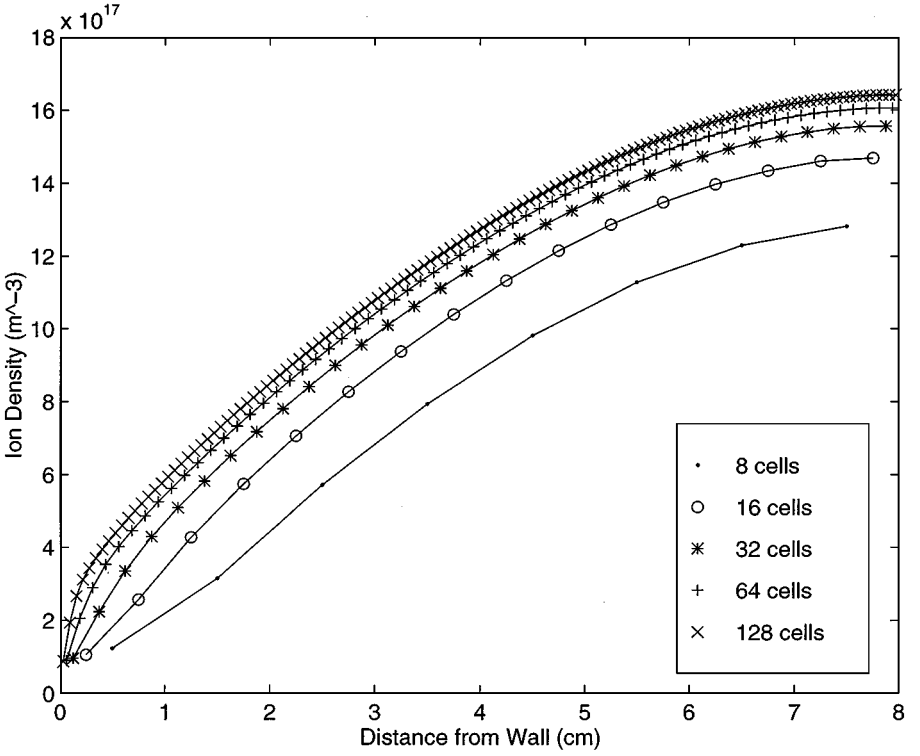


**FIG. 6.** Ion density profiles (number per cubic meter).

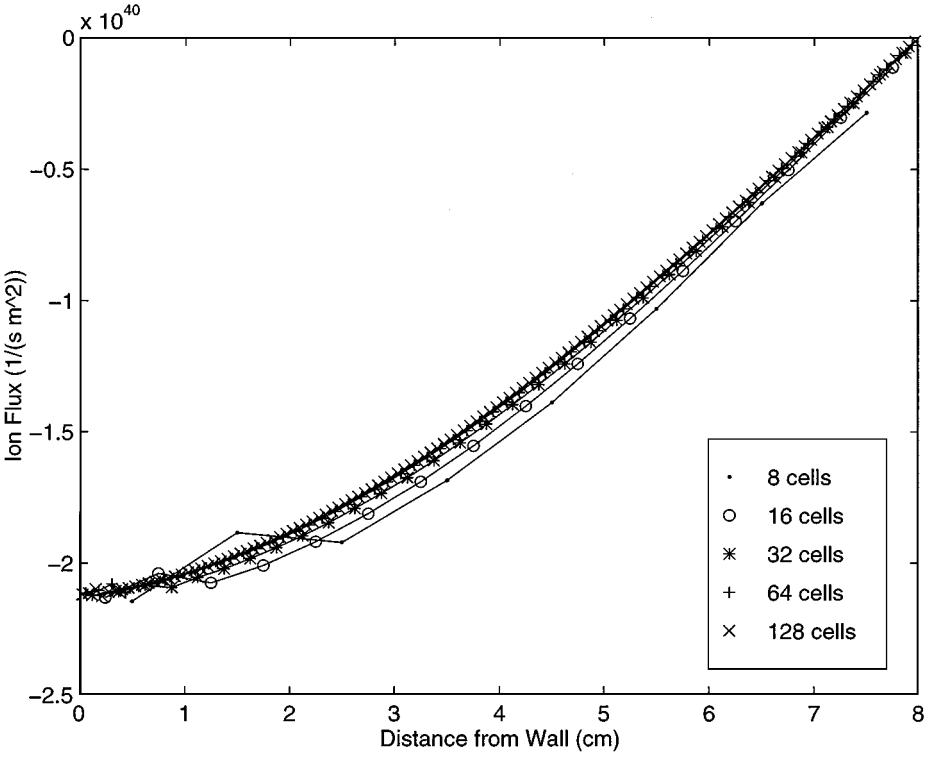


**FIG. 7.** Ion flux profiles (number per square meter second).

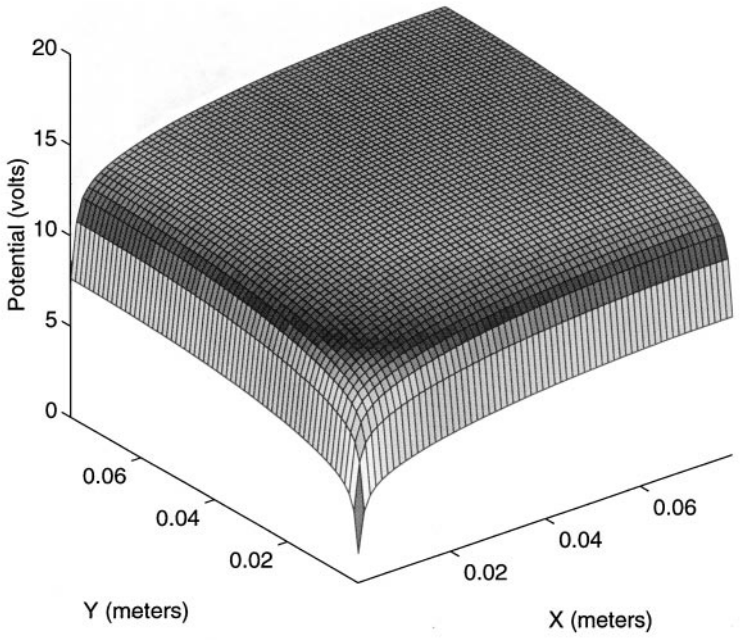


**FIG. 8.** Potential profile for sample calculation.

is an 8-cm square that is grounded along two adjacent sides with symmetry boundary conditions applied to the other two sides. A $64 \times 64$ spatial grid is imposed.

The timestep restriction (3.80) for the algorithm described in Section 3 is determined by the mesh size and the peak electron drift velocity. The limit for a purely explicit treatment would be the dielectric relaxation timestep limit (which is grid independent). Regardless of the method used to integrate the electrons and potential, we are still bound by the Courant condition determined by the ion velocity if we use an explicit method for the ion advection. Therefore, the Courant limit imposed by the ion velocity can be viewed as the theoretical limit for large timestep selection. In Table III we have tabulated these limiting timesteps at steady state for this sample problem. The values for the "quasineutral" data were determined at the center of the spatial domain, and the "sheath" data was extracted from a cell along the physical boundary. In order to emphasize the difference in timestep selection for a steady state solution, we have also tabulated the number of timesteps required

**TABLE III**
**Comparison of Computational Complexity for Different Limiting Timesteps**

| Factor limiting timestep | Timestep (seconds) | Number of steps to steady state |
|---|---|---|
| Ion Courant condition (quasineutral region) | 4.89e-6 | 102 |
| Ion Courant condition (sheath region) | 1.77e-7 | 2,825 |
| Electron drift velocity Courant condition (quasineutral region) | 1.64e-8 | 30,487 |
| Electron drift velocity Courant condition (sheath region) | 2.03e-10 | 2,463,054 |
| Dielectric relaxation time | 2.50e-15 | 200,000,000,000 |

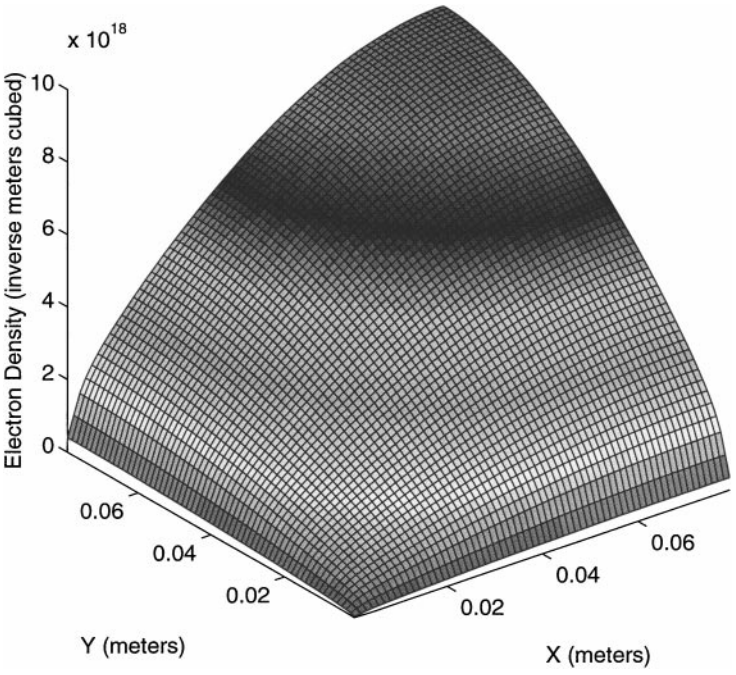


**FIG. 9.** Electron density profile for sample calculation.

to integrate the plasma system to 500 $\mu$s. This shows that, despite the removal of the dielectric relaxation timestep limit, the electron drift timestep limit remains and makes the calculation of steady state solutions difficult. We are currently working toward removing this limit as well, and our goal is to push the timestep stability limit to that required for the ion advection.

Stability is not the only issue, of course. Typical ICP reactors utilize a 13.56 MHz radio frequency (rf) bias potential on the wafer surface, in order to independently control ion density and energy flux. Timesteps much smaller than the rf period must be used in order to accurately resolve the bias effects [16]. In this case, the ion limiting timestep may be too large because of insufficient temporal accuracy. Even in this case, however, the electron drift-limiting timestep is smaller than necessary from an accuracy point of view. It is also possible that transient behavior may be of interest, although we have not explored this issue.

## 5. CONCLUSION

We have presented a new numerical method for the solution of a set of plasma fluid equations similar to those used in modeling semiconductor fabrication processes. In addition to a careful temporal splitting of the full fluid system, higher-order spatial discretizations were applied in an effort to reduce the amount of spatial gridding relative to lower order discretizations. The results of Section 4 clearly demonstrate the need for a more aggressive gridding strategy near the sheath boundary layer. As mentioned in the Introduction, the Cartesian grid algorithm presented here can be used as a refinement level integrator in a locally refined grid algorithm [4].

## ACKNOWLEDGMENTS

We thank Peter Vitello at Lawrence Livermore National Laboratory (LLNL) for his many helpful discussions regarding plasma modeling. We also acknowledge the assistance of Xabier Garaizar, also at LLNL, in the formulation of the modified Euler equations. Finally, we thank the reviewers for suggesting several important additions to the manuscript.

## REFERENCES

1. M. S. Barnes, T. J. Colter, and E. Elta, Large-signal time-domain modeling of low-pressure RF glow discharges, *J. Appl. Phys.* **61**, 81 (1987).
2. F. F. Chen, *Introduction to Plasma Physics and Controlled Fusion* (Plenum, New York, 1984).
3. P. Colella, Multidimensional upwind methods for hyperbolic conservation laws, *J. Comput. Phys.* **87**, 171 (1990).
4. P. Colella, M. R. Dorr, and D. D. Wake, *Numerical Solution of Plasma Fluid Equations Using Locally Refined Grids*, Technical Report UCRL-JC-129913, Lawrence Livermore National Laboratory, Livermore, California, March 1998. [*J. Comput. Phys.*, submitted]
5. P. Colella and E. G. Puckett, *Modern Numerical Methods for Fluid Flow* (Cambridge Univ. Press, Cambridge), in preparation.
6. G. Dahlquist and A. Bjorck, *Numerical Methods* (Prentice-Hall, Englewood Cliffs, NJ, 1974).
7. L. R. Peterson and J. E. Allen, Jr., Argon elastic scattering and ionization rates, *J. Chem. Phys.* **56**(12), 6068 (1972).
8. V. E. Golant, A. P. Zhilinsky, and I. E. Sakharov, *Fundamentals of Plasma Physics* (Wiley, New York, 1980).
9. S. Hashiguchi, Implicit difference scheme to calculate electric fields, *Japan. J. Appl. Phys.* **32**(1A/B, 15), L138 (1993).
10. R. J. LeVeque, *Numerical Methods for Conservation Laws* (Birkhauser, Basel, 1992).
11. M. A. Lieberman and A. J. Lichtenberg, *Principles of Plasma Discharges and Materials Processing* (Wiley, New York, 1994).
12. D. M. Manos and D. L. Flamm, *Plasma Etching: An Introduction* (Academic Press, San Diego, 1989).
13. R. A. Stewart, P. Vitello, and D. B. Graves, Two-dimensional fluid model of high density inductively coupled plasma sources, *J. Vacuum Sci. Technol. B* **12** (1994).
14. G. Strang, On the construction and comparison of difference schemes, *SIAM J. Numer. Anal.* **5**, 506 (1968).
15. N. Tishchenko, personal communication.
16. P. Vitello, personal communication.
17. D. D. Wake, *Simulation of Plasma Based Semiconductor Manufacturing Using Block Structured Locally Refined Grids*, Ph.D. thesis, University of California, Davis, 1998.